LCLS-II Technical Note

LCLS-II start-to-end simulations as of August 2015

LCLS-II TN-15-33

[Publish Date]

G. Marcus, J. Qiang

1 Introduction

This technical note details the current status of the LCLS-II start-to-end simulations as of August 2015. All of the FEL simulations use the electron beam distributions from the July 2015 IMPACT start-to-undulator release.

2 FEL performance table

A detailed description of the simulations leading to the FEL performance table can be found in the attached papers.

	SXR			HXR		
	250eV	**750eV**	**1.25keV**	**1.5keV**	**3.25keV**	**5keV**
20pC (1.5 MHz)	267 (42), 35, 3, 8, 400, 32, (297, 307), (16.5, 16.9)	239 (43), 32, 6.5, 8, 360, 26, (104, 105), (7.10, 7.31)	168 (41), 38, 8, 4, 250, 20, (59, 57), (4.52, 4.55)	206 (27), 34, 4.5, 6, 310, 72, (79, 83), (4.11, 4.20)	147 (22), 39, 7, 4, 220, 50, (51, 49), (1.71, 1.72)	25 (7), 17, -, 1.5, 38, 24, (29, 29), (1.49, 1.52)
100pC (300 Hz)	1205 (260), 52, 3, 23, 360, 34, (290, 245), (13.74, 11.60)	795 (135), 50, 6, 16, 240, 28, (95, 77), (5.61, 5.30)	527 (76), 43, 6, 12, 160, 22, (57, 54), (3.59, 3.40)	1136 (111), 45, 5, 25, 340, 62, (79, 78), (2.94, 2.86)	469 (46), 46, 8, 10, 140, 40, (51, 51), (1.54, 1.56)	10 (6), 25, 10, 0.5, 3, 14, (52, 53), (2.49, 2.54)
300pC (100 kHz)	5482 (1013), 252, 4, 22, 550, 40, (178, 164), (9.76, 9.10)	3844 (519), 215, 4, 18, 380, 20, (62, 65), (4.83, 4.68)	1897 (422), 150, 4, 13, 190, 16, (42, 39), (3.56, 3.62)	2364 (300), 130, 3, 18, 240, 62, (70, 65), (2.93, 2.66)	642 (147), 120, 3.5, 5, 64, 40, (45, 43), (1.65, 1.56)	- (0.4) , -, -, -, -, -, -, -

LCLS-II Performance Table: E (µJ), () - @ saturation, Δt_{FWHM} (fs), ΔE_γ (eV), P_{pk} (GW), P_{avg} (W), Z_0 (m), σ_{RMS} (x,y) (µm), Θ_{RMS} (x,y) (µrad)

START-TO-END SIMULATION OF THE LCLS-II BEAM DELIVERY SYSTEM WITH REAL NUMBER OF ELECTRONS*

J. Qiang[#], M. Venturini, C. Mitchell, C. Papadopoulos, LBNL, Berkeley, CA94720, U.S.A.
Y. Ding, P. Emma, Z. Huang, G. Marcus, Y. Nosochkov, T. O. Raubenheimer, L. Wang, M. Woodley, SLAC, Menlo Park, CA 94025, U.S.A.

Abstract

The LCLS-II as a next generation high repetition rate FEL based X-ray light source will enable significant scientific discoveries. In this paper, we report on progress in the design of the accelerator beam delivery system through start-to-end simulations. We will present simulation results for three charges, 20 pC, 100 pC and 300 pC that are transported through both the hard X-ray beam line and the soft X-ray beam line for FEL radiation.

INTRODUCTION

Next generation high brightness FEL X-ray light sources provide great opportunity for scientific discovery in many fields. The LCLS-II as an upgrade to the current LCLS FEL at SLAC will deliver photons of energy between 200 eV and 5 keV at a repetition rate as high as 1 MHz and is being actively designed under a multi-laboratory collaboration [1]. Figure 1 shows a schematic layout of the LCLS-II beam delivery system [2]. It consists of a high repetition rate photo-injector to generate and accelerate the electron beam to 100 MeV, a laser heater (LH) to suppress microbunching instability, a section of superconducting linac L1 to accelerate the beam to 250 MeV, a bunch compressor BC1, a second section of superconducting linac L2 to accelerate the beam to 1.6 GeV, a bunch compressor BC2, and a third section of superconducting linac L3 to accelerate the beam to 4 GeV, a long bypass transport line, and a magnetic kicker to spread the electron beam to a soft X-ray transport beam line and to a hard X-ray transport beam line. The superconduting linacs in all three sections are made of 1.3 GHz 9 cell superconducting cavities except the two cryomodules of 3.9 GHz third harmonic cavities right before the BC1 to linearize longitudinal phase space.
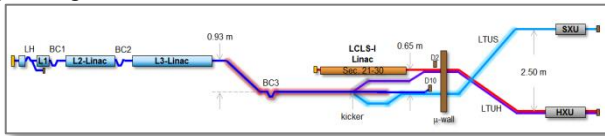

Fig. 1: A schematic layout of the LCLS-II.

COMPUTATIONAL SETUP

All simulations presented in this study were done using a 3D parallel beam dynamics simulation framework IMPACT [3-5]. It includes a time-dependent 3D space-charge code module IMPACT-T to simulate photo-electron beam generation and acceleration through the photo RF gun, buncher and boosting cavities, and a position-dependent 3D space-charge code module to simulate electron beam transport through the superconducting linac system. Besides the 3D space-charge effects, the simulation also includes coherent synchrotron radiation (CSR) effects through a bending magnet, incoherent synchrotron radiation inside the bending magnet, RF cavity structure wakefield, and resistive wall wakefield. All simulations were done using the real number of electrons for three bunch charges, 20 pC, 100pC, and 300pC, to capture the initial shot noise of the beam, which can have important impact on the final beam quality and FEL performance due to the microbunching instability [6-8]. The total computational time takes from a few hours to about 14 hours on thousands of processors at the NERSC supercomputer center [9].

SIMULATION RESULTS

The simulation starts with an initial particle distribution behind the cathode. The choice of the initial electron beam parameters and the RF gun, the solenoid, the buncher cavity, and the boosting cavities parameters was based on a multi-variable multi-objective optimization [10]. Figure 2 shows the longitudinal phase space distribution and the current profile at the exit of the
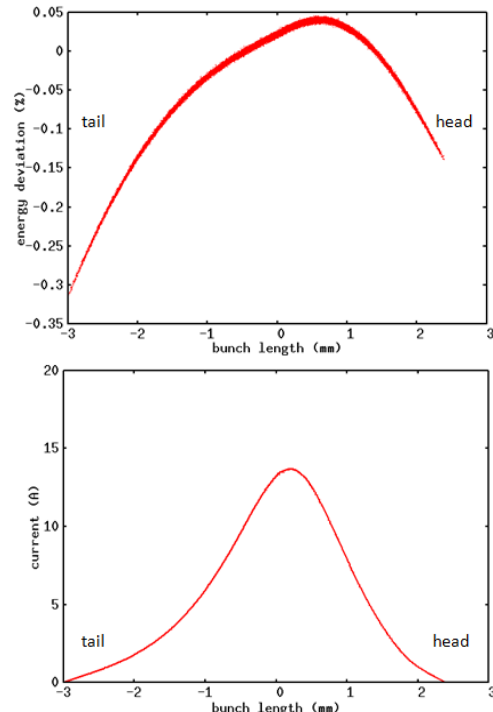

Fig. 2: Longitudinal phase space (top) and current profile (bottom) at the exit of the injector.

injector for the nominal 100 pC charge case. The relative energy deviation in the longitudinal phase space is small but with noticeable nonlinear component that might affect the final beam compression. The peak current of the beam at this location is about 14 Ampere.

The electron beam coming out of the injector is sent through a laser heater chicane to increase its uncorrelated energy spread to suppress the microbunching instability. A detailed discussion of the microbunching instability in the LCLS-II is presented in the reference [6] of these proceedings. For the nominal 100 pC charge, we assumed a 7 keV increase of uncorrelated energy spread from the laser heater. After the laser heater, the electron beam is transported through the first section of the superconducting linac, the third harmonic linearizer, and the bunch compressor chicane BC1 to boost the beam energy and to increase the peak current. The RF accelerating gradient and the phase used in this section of linac are 12.72 MV/m and -12.7 degree respectively. The accelerating gradient and the phase used in the third harmonic cavity are 11.69 MV/m and -150 degree respectively. The bunch compressor BC1 has a compression factor of 6. The bending angle in this chicane is 0.1028 radian and the R56 of the chicane is 0.055 meters. Figure 3 shows the longitudinal phase space and the current profile after the BC1. The longitudinal phase space looks quite linear. The peak current is about 85 A with noticeable modulation due to the microbunching instability. After the BC1, the beam is further accelerated through the second section of the superconducting linac to 1.6 GeV before entering the second bunch compressor BC2. The accelerating gradient and the phase in this section of linac are 14.51 MV/m and -21 degree respectively. The bending angle in BC2 is 0.043 radian and the R56 of the chicane is 0.0379 m. This provides another compression factor of 8 to the beam.
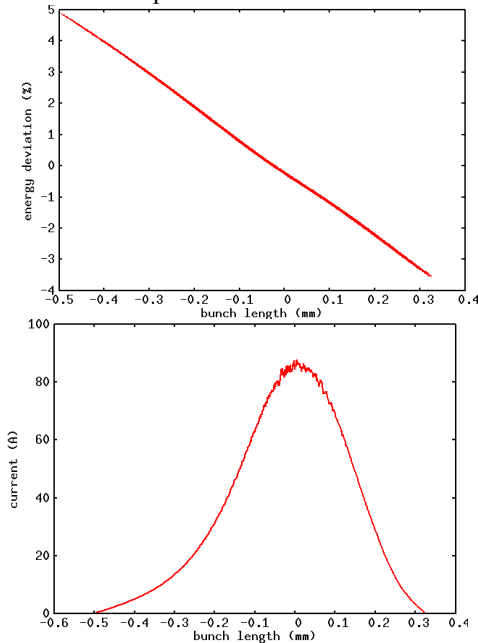

Fig. 3: Longitudinal phase space (top) and current profile (bottom) at the exit of the BC1.

Figure 4 shows the longitudinal phase space distribution and the current profile after the BC2. Nonlinear tail forms around both ends of the beam and contributes to two large spikes in the current profile.

After the BC2, the electron beam is further accelerated through the third section of the superconducting linac to reach 4 GeV energy before entering the long transport beam line to the undulator hall. The RF gradient and the phase used in this section of linac are 14.71 MV/m and 0 degree respectively. The long transport beam line consists of a dogleg 1, a long bypass, and a spreader to a soft X-ray transport line and to a hard X-ray transport line. The final longitudinal phase spaces and the current profiles at the entrance to the soft X-ray FEL and the hard X-ray FEL are given in Figs. 5 and 6. Compared with the Fig. 4, the final longitudinal phase distribution becomes flatter and is dechirped by the resistive wakefield through the long transport line. The flat core of the beam is about 13 um with relatively small energy and current modulation due to the microbunching instability. Such a modulation might not present significant impact to the SASE FEL performance but can degrade the performance of the seeded FEL. The current and the energy modulation in the beam at the entrance to the soft X-ray FEL are worse than that at the entrance to the hard X-ray FEL. Study is ongoing to further improve both the soft X-ray and the hard X-ray transport beam lines to minimize the microbunching effects at the entrance to the undulator.
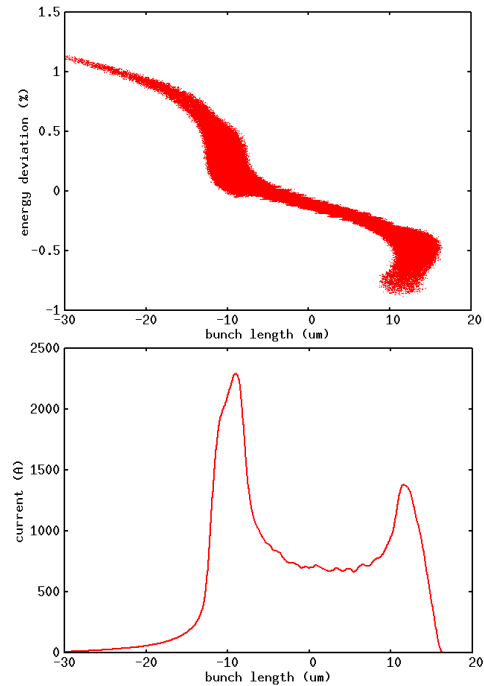

Fig. 4: Longitudinal phase space (top) and current profile (bottom) at the exit of the BC2.

Figure 7 shows the transverse projected rms emittance evolution and the transverse center slice emittance (averaged over 5 slices) evolution through the linac and the hard X-ray transport beam line for the nominal 100pC charge case. Some large spikes in the emittance are due to the dispersion inside a chicane or a dogleg. The large

projected rms emittance growth after the BC2 and the final dogleg is due to the CSR effects caused by these large current spikes in the beam. Some slice emittance growth is also noticed after the BC1 due to the nonlinear space-charge effects associated with the lattice mismatch and the strong focusing of the beam around this region. The final slice emittances in both horizontal (X) and veritical (X) planes are below 0.5 um. The projected X
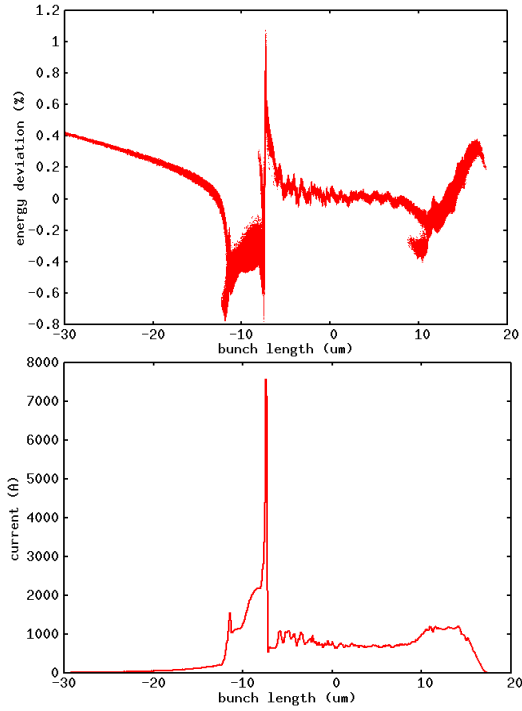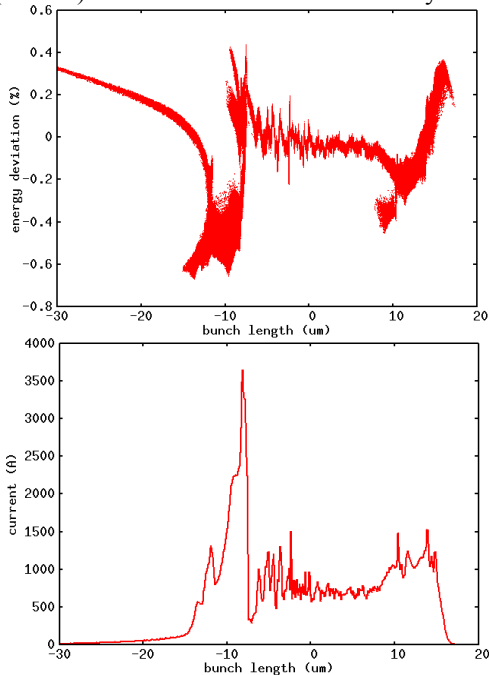
emittance is about 1um and the projected Y emittance is about 0.5 um.

Besides the nominal 100 pC charge case, we also carried out start-to-end simulation using the real number of electrons for the 300 pC charge and the 20 pC charge. Figure 8 shows the final longitudinal phase space and current profile at the entrance to the hard X-ray FEL for the 300 pC charge. The core of the beam has about 60 um relatively flat distribution with a current beyond 800 A. The final projected transverse emittance is about 1.3 um

Fig. 5: Longitudinal phase space (top) and current profile (bottom) at the entrance to the hard X-ray FEL.

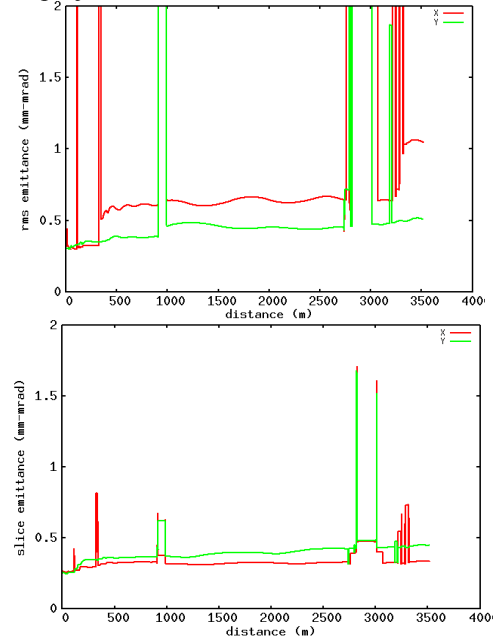Fig. 7: Transverse projected RMS emittance evolution (top) and slice emittance evolution (bottom) through the hard X-ray beam delivery system.

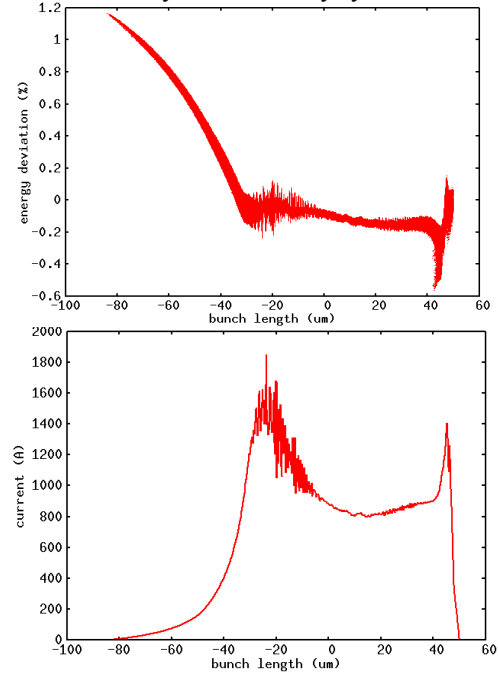

Fig. 6: Longitudinal phase space (top) and current profile (bottom) at the entrance to the soft X-ray FEL.

Fig. 8: Final longitudinal phase space (top) and current profile (bottom) for the hard X-ray FEL with 300 pC.

in X and 0.94 um in Y. The center slice emittance is about 0.63 um in X and 0.59 um in Y. Similar phase space distribution and current profile are also obtained for the beam through the soft X-ray transport line.
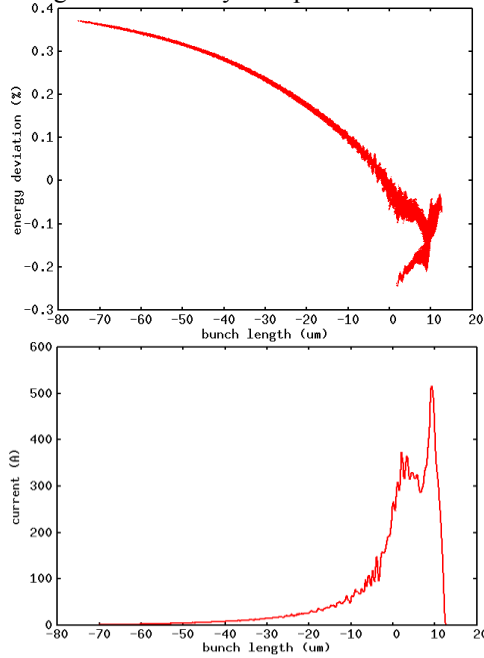

Fig. 9: Final longitudinal phase space (top) and current profile (bottom) for the hard X-ray FEL with 20 pC.

Figure 9 shows the final longitudinal phase space and the current profile at the entrance to the hard X-ray FEL for the 20 pC charge case. The peak current in the core of the distribution is about 300 A with a length of about 9 um. The final projected rms emittances are 0.21 um in X and 0.13 in X. The center slice emittances are 0.13 um and 0.12 um in X and Y planes respectively.

SUMMARY AND DISCUSSIONS

As a summary, Table I gives some final beam parameters at the entrance to both the hard X-ray FEL (blue) and the soft X-ray FEL (brown) from the start-to-end simulations using real number of electrons. Those parameters that are important to the FEL performance include peak current inside the core, uncorrelated energy spread inside the core, total projected transverse RMS emittances, and core slice emittances. The 300 pC charge gives the largest ~900 A peak current inside the core of the beam. The nominal 100 pC charge leads to a final ~750 A peak current, and the 20 pC charge produces ~300 A peak current inside the core of the beam. The final transverse core slice emittances are below 1 um for all three charges. The total projected RMS emttiances are around 1 um for 100 pC and 300 pC charges except the one with 100pC charge after the soft X-ray beam line. This large total projected emittance is due to the large fish tail shape distribution in the longitudinal-horizontal plane around the tail of the beam where a large energy tail is also observed in the top plot of the Fig. 6. This part of the beam might not contribute to the desired FEL radiation

from the core of the beam in the downstream undulator. The final uncorrelated rms energy spread is below 600 keV for all three bunch charges.

Table I: Final beam parameters at the entrance to the hard X-ray FEL (blue) and the soft X-ray FEL (brown)

IMPACT Studies	I_peak (A)	σ_E (keV)	Proj. $\varepsilon_x / \varepsilon_y$ (mm-mrad)	Slice $\varepsilon_x / \varepsilon_y$ (mm-mrad)
20 pC	299	446	0.21/ 0.13	0.16 / 0.10
	294	444	0.23 / 0.12	0.15 / 0.10
100 pC	760	480	1.05 / 0.51	0.34 / 0.43
	755	592	3.5 / 0.44	0.34 / 0.42
300 pC	892	468	1.28 / 0.94	0.64/ 0.52
	921	529	1.21 / 0.90	0.56 / 0.53

The electron beam quality parameters listed in the Table I result in a reasonable FEL performance in the downstream undulators[7]. Further improvement to the quality of the beam is still undergoing. For example, recently, we have optimized the settings of the compensation chicane to further reduce the microbunching instability effects through the long transport line. We are also working on improving the beam current profile and reducing the microbunching effects by using a third bunch compressor right before the spreader. This bunch compressor helps to lower the compression factor needed in the first two stages and the peak current through the long bypass, which in principle will reduce the growth of the microbunching instability. This bunch compressor was used in the 20 pC charge case presented here. The challenge with this delayed compression is to remove the longitudinal energy chirp in the final beam distribution since the distance to the undulator entrance is short and the resistive wall wakefield might not be large enough to remove the energy chirp. Besides improving the longitudinal energy/density profile, we are also working on understanding the transverse emittance growth in the linac.

REFERENCES

[1] T. O. Raubenheimer, "Technical challenges of the LCLS-II CW X-ray FEL," in proceedings of IPAC2015, Richmod, VA, USA.
[2] P. Emma et al., in proceedings of FEL'14, THP025.
[3] J. Qiang et al., PRST-AB 9, 044204 (2006).
[4] J. Qiang et al., J. of Comp. Phys., 163, 434 (2000).
[5] J. Qiang et al., PRST-AB 12, 100702 (2009).
[6] J. Qiang et al., PRST-AB 17, 030701 (2014).
[7] M. Venturini et al., "The microbunching instability and LCLS-II lattice design: lessons learned," in these proceedings.
[8] G. Marcus et al., "High fidelity start-to-end numerical particle simulations and performance studies for LCLS-II," in these proceedings.
[9] http://www.nersc.gov.
[10] C. Papadopoulos et al, "RF injector beam dynamics optimization for LCLS-II," SLAC-PUB-16210 (2014).

HIGH FIDELITY START-TO-END NUMERICAL PARTICLE SIMULATIONS AND PERFORMANCE STUDIES FOR LCLS-II

G. Marcus, Y. Ding, P. Emma, Z. Huang, T. O. Raubenheimer, L. Wang
SLAC, Menlo Park, CA 94025, USA

J. Qiang, M. Venturini
LBNL, Berkeley, CA 94720, USA

Abstract

High fidelity numerical particle simulations that leverage a number of accelerator and FEL codes have been used to analyze the LCLS-II FEL performance. Together, the physics models that are included in these codes have been crucial in identifying, understanding, and mitigating a number of potential hazards that can adversely affect the FEL performance, some of which are discussed in papers submitted to this conference [1, 2]. Here, we present a broad overview of the LCLS-II FEL performance, based on these start-to-end simulations, for both the soft X-ray and hard X-ray undulators including both SASE and self-seeded operational modes.

INTRODUCTION

The LCLS-II is an advanced x-ray FEL light source that consists of two independently tunable undulators capable of producing radiation covering a large spectral range that can be fed by both a CW superconducting RF (SCRF) linac or by the existing copper linac [3]. Each undulator beamline will be dedicated to the production of either hard (HXR) or soft (SXR) x-ray photons and will incorporate self-seeding [4, 5] infrastructure to produce narrow-bandwidth and longitudinally coherent FEL pulses. Addtional details regarding the baseline design can be found elsewhere [3, 6, 7].

It has been found that the relatively low electron beam energy of 4 GeV (compared to the nominal operation of LCLS) along with an extended transport distance from the end of the linac to the entrance of the undulators leaves the electron beam susceptible to a space-charge driven microbunching instability (MBI) [8–10]. This MBI manifests as large slice current and energy modulations that can potentially degrade the FEL performance. In addition, the space-charge MBI is the leading candidate responsible for the production of a self-seeded spectral 'pedestal' which is seen in both experiment [11] and in simulation [13] and is the topic of current theoretical study [2, 12].

This paper reports the results of high fidelity numerical particle simulations using the suite of codes IMPACT [14–16] and GENESIS [17]. These simulations include the effects of three-dimenstonal space charge, coherent and incoherent synchrotron radiation, RF cavity wakefields and resistive wall wakefields in the generation, acceleration and transport of the electron beam from the cathode to the undulator for three charge distributions: 20 pC, 100 pC, and 300 pC. To model the initial shot noise of the electron beam, which may act as the seed for the space-charge driven MBI, the real number of electrons were tracked from the cathode. The various charge distributions were then used to define the electron beams in GENESIS, where resistive wall wakefield effects are also included in the FEL simulations. SASE has been studied across the tuning ranges for each of the individual charge distributions for both the HXR and SXR undulators and include fully time-dependent taper optimizations. Preliminary results for self-seeding with the 100 pC electron beam will also be discussed.

ELECTRON BEAM PROPERTIES

A detailed start-to-end simulation study of the accelerator beam delivery system is reported elsewhere [1, 18]. Below, we present the electron beam longitudinal phase space (LPS) and critical slice parameters for each of the charge distributions discussed above at the entrance to the SXR undulator. The LPS of the electron beams at the entrance to the HXR undulator show less effects of MBI for reasons discussed in [18]. This sets the stage for detailed FEL simulations in the following section.

20 pC

Figure 1 shows the LPS along with various slice properties of the 20 pC electron beam that has been tracked to the SXR undulator. The core of the distribution is roughly 8 μm long,
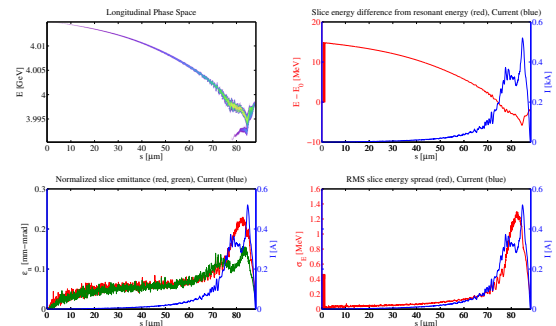

Figure 1: Slice properties of the 20 pC electron beam that has been tracked to the SXR undulator. Top left: longitudinal phase space; top right: slice energy deviation from the resonant energy (red) and current (blue); bottom left: normalized slice emittance (x-red, y-green) and current (blue); bottom right: rms slice energy spread (red) and current (blue).

is slightly chirped with the head of the beam having a lower

energy, and has a $I \sim 300$ A current. The normalized slice emittance is less than $\epsilon_n \sim 0.2$ μm in both transverse planes, so while the current is rather low, the beam is sufficiently bright such that it can produce greater than 20 μJ of energy per pulse at the high end of the tuning range in the HXR undulator (5 keV), which is important for operations. The rms slice energy spread in the core of the beam reads as greater than $\sigma_E \sim 1.2$ MeV, but is really closer to $\sigma_E \sim 0.45$ MeV if one neglects the filamentation seen in the LPS from the calculation.

100 pC

Figure 2 shows the LPS along with various slice properties of the 100 pC electron beam that has been tracked to the SXR undulator. It is obvious that the space-charge driven
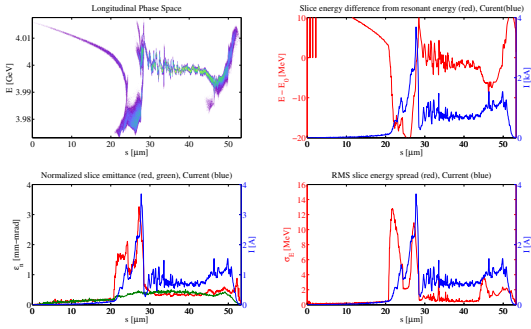

Figure 2: Slice properties of the 100 pC electron beam that has been tracked to the SXR undulator. Top left: longitudinal phase space; top right: slice energy deviation from the resonant energy (red) and current (blue); bottom left: normalized slice emittance (x-red, y-green) and current (blue); bottom right: rms slice energy spread (red) and current (blue).

MBI has severely impacted the LPS of the beam where large current and energy variations can be seen along the longitudinal profile. Nevertheless, the current in the core, which is roughly 20 μm long, is about $I \sim 750$ A. Peak to peak energy variations along the longitudinal profile can be as large as 8 MeV just after the large current spike in the tail of the beam. The normalized slice emittance is less than $\epsilon_n \sim 0.43$ μm in both transverse planes while the rms slice energy spread is roughly $\sigma_E \sim 0.55$ MeV.

300pC

Figure 3 shows the LPS along with various slice properties of the 300 pC electron beam that has been tracked to the SXR undulator. The core of this distribution, which is less impacted by the space-charge induced MBI than the 100 pC electron beam, is roughly 50 μm long and has a current of $I \sim 900$ A. The normalized slice emittance is less than $\epsilon_n \sim 0.70$ μm in both transverse planes while the rms slice energy spread is roughly $\sigma_E \sim 0.40$ MeV. While the larger transverse emittance for this charge distribution will negatively impact the performance at the high end of the tuning range of the HXR undulator, the relatively flat LPS in
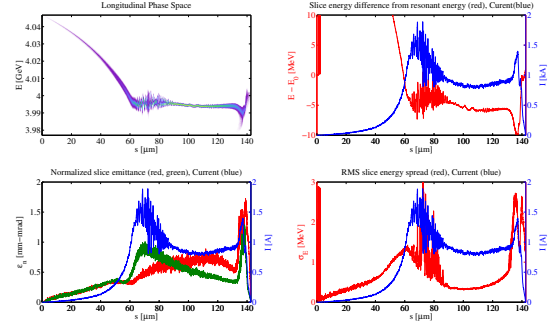

Figure 3: Slice properties of the 300 pC electron beam that has been tracked to the SXR undulator. Top left: longitudinal phase space; top right: slice energy deviation from the resonant energy (red) and current (blue); bottom left: normalized slice emittance (x-red, y-green) and current (blue); bottom right: rms slice energy spread (red) and current (blue).

the core may be useful for self-seeded or externally seeded applications [13].

SASE PERFORMANCE STUDY

Undulator parameters

Details of the undulator layout can be found elsewhere [6, 7]. Figure 4 shows the main parameters of the HXR and SXR undulators. The undulator vacuum chamber will be

Parameter	Value SXR (HXR)	Unit
Type	Hybrid PM, planar	-
Full gap height	Variable	-
Period	39 (26)	mm
Segment length	3.4	m
Break length	1.0	m
# segments	21 (32)	-
Total length	96 (140)	m

Figure 4: LCLS-II undulator parameters

made of aluminum and will have a rectangular cross section with a 5 mm gap height, which is used to define the resistive wall wakefield for the FEL simulations.

Tapering optimization and performance

The tapering scheme employed here follows the strategy laid out in [19] and is based on a three parameter optimization (z_0, ξ, d) of the final FEL pulse energy. Here the taper is given by

$$a_w(z) = a_w(z_0) \times \left[1 - c(z - z_0)^d\right], \qquad (1)$$

where z_0 is the taper starting location, which is typically a few power gain lengths before saturation; $c = \frac{\xi}{(L_w - z_0)^d}$,

	SXR			HXR		
	250eV	750eV	1.25keV	1.5keV	3.25keV	5keV
20pC	267 (42)	239 (43)	168 (41)	206 (27)	147 (22)	25 (7)
100pC	1205 (260)	795 (135)	527 (76)	1136 (111)	469 (46)	10 (6)
300pC	5482 (1013)	3844 (519)	1897 (422)	2364 (300)	642 (147)	- (0.4)

Figure 5: LCLS-II start-to-end SASE performance study with optimized post-saturation tapering. The left column indicates the electron beam charge while the top two rows indicate either the SXR or HXR undulator and the photon energy in each undulator that was studied. The parentheses indicate the energy at saturation, which is not necessarily the energy at the end of the undulator without a post-saturation taper.

where $\xi = 1 - \frac{a_w(L_w)}{a_w(z_0)}$ is the taper ratio (the % change of the rms undulator parameter a_w over the tapered part of the undulator) and L_w is the length of the tapered part of the undulator; and d is the taper profile order. Full time-dependent (not single slice or single frequency) taper optimizations are needed in order to capture the dynamics of SASE in the post-saturation regime accurately. The optimal taper that is nominally given by single-slice optimization scans over the three parameters listed above is more appropriate for seeded FELs. This is because particles in distinct coherence regions (SASE spikes) tend to have uncorrelated ponderomotive phases [20]. We have found that the optimal taper given by a single-slice parameter scan often produces less than half the energy that could be achieved by a full time-dependent parameter scan, which is a significant result. Figure 6 shows the result of a typical parameter scan for the 100 pC electron beam resonant at $E_\gamma = 1.5$ keV in the HXR undulator for one particular taper starting location, z_0. The taper profile order, d, is typically around 2 and the optimal taper ratio, ξ, depends on the undulator length and various electron beam and radiation properties. A summary of the LCLS-II SASE performance with post-saturation tapering can be found in Figure 5 for the charge distributions and tuning ranges that span the relevant parameter spaces. The FEL seems to be insensitive to the MBI induced energy and current modulations at all but highest photon energies in the HXR undulator, where the beam is more sensitive to slice energy spread.

SELF-SEEDED PERFORMANCE STUDY

Simulation strategy

The SXR beamline will incorporate a self-seeding system (SXRSS) to produce longitudinally coherent soft x-ray free electron laser pulses. It will consist of two undulators that are separated by a monochromator and a magnetic chicane. The first undulator will consist of 7-8 independent segments while the second undulator consists of 13-14 independent segments. The monochromator design will be based on the existing LCLS SXRSS monochromator [21] with additional flexibility built in. It will have a compact footprint that is designed to allow both the chicane and monochromator to
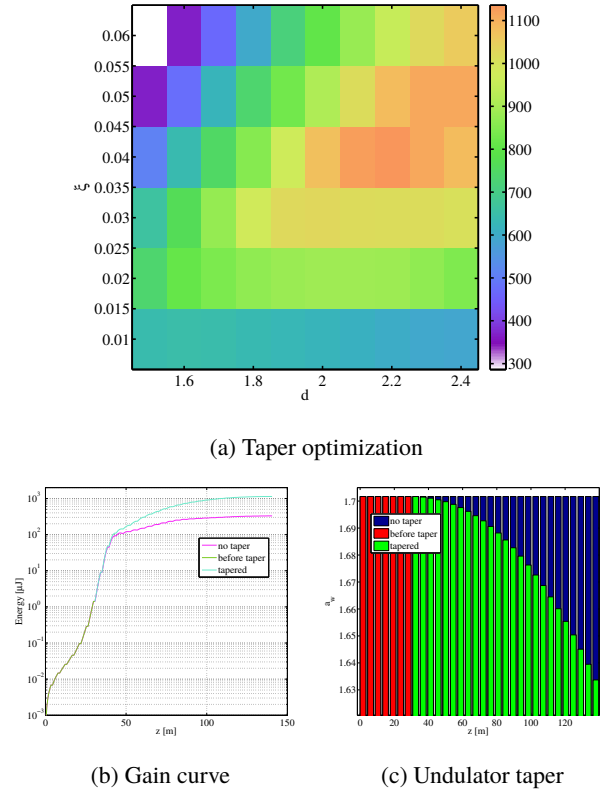

(a) Taper optimization

(b) Gain curve

(c) Undulator taper

Figure 6: (a) taper optimization showing the energy at the end of the undulator as a function of d and ξ; (b) gain curve for the optimal taper and for the un-tapered case; (c) the taper profiles for the optimal taper and the un-tapered case

occupy the equivalent space of a single undulator segment along the strong focusing quadrupole FODO cell strongback. The resolving power is nominally specified to be $R = 15,000$, but upgrade paths to $R \sim 30,000$ are being explored.

The specification of the individual components of both the monochromator and chicane are not yet established. As such, a phenomenological approach is used to model the bandwidth reduction of the seed. The nominal monochromator design relative bandwidth $(1/R)$ and overall efficiency ($\sim 5\%$) are used to specify the amplitude of a Gaussian fre-

(a) Energy gain curve   (b) Power

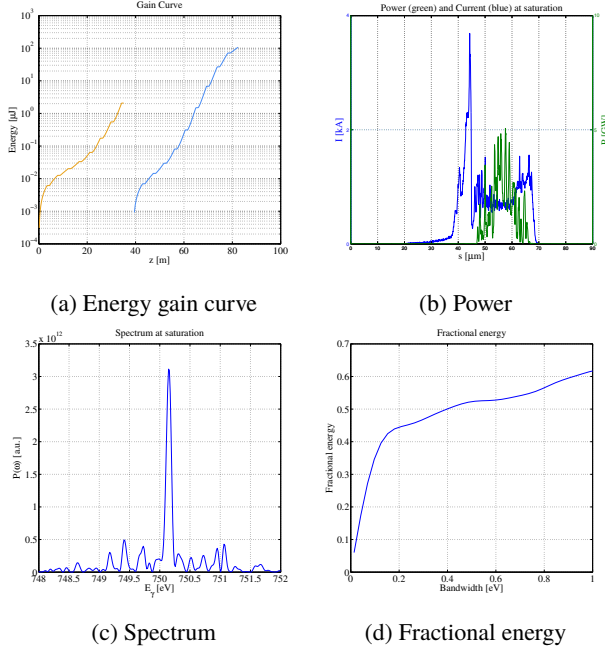(c) Spectrum   (d) Fractional energy

Figure 7: (a) Energy gain curve for the SASE undulator (orange) which generates the seed to be monochromatized and amplified downstream (blue); (b) Power (green) and current (blue) at saturation; (c) On-axis spectrum at saturation; (d) Fractional energy within a given bandwidth at saturation.

quency filter function. The phase of the filter function is defined through Kramers-Kronig relations such that causality is not violated when the filter is applied to the fully three-dimensional FEL pulse exiting the seventh or eigth undulator section. The fields exiting the monochromator are then used to specify the seed into the next undulator. Diffraction through the actual monochromator setup is not modeled. This is, however, a small effect at these photon energies. In addition, a new and simple optical propagation theory has been developed to track the full three-dimensional field through the optical lattice and will be explored when the monochromator design has matured [22].

The magnetic chicane serves the dual role of compensating for the delay introduced by the monochromator and destroying any residual electron beam microbunching from the first undulator. This is modeled in a very simple way by using the dumped particle distribution and re-initializing the shotnoise.

Performance

The nominal performance for the SXRSS system using the 100 pC electron beam distribution tuned to produce $E_\gamma = 750$ eV photons is illustrated in Figure 7. The first undulator terminates the field growth well before saturation after 8 undulator sections (orange, Figure 7a). Here, the FEL energy is roughly 2 μJ while the longitudinal profile in both the spectral and temporal domain display the typical SASE spiking. The field is then frequency filtered while the electron beam shotnoise is re-initialized according to

the description above. The field is amplified to saturation in a downstream undulator (blue, Figure 7a). The temporal duration at this point is roughly $\Delta T_{FWHM} \sim 36$ fs (Green, Figure 7b), which is consistent with the resolving power of $R = 15,000$ at this photon energy. Some spiking due to the fluctuating electron beam slice properties is evident. The spectrum at this point (Figure 7c) has a dominant spike with a spectral width $\Delta E_\gamma \sim 100$ meV, which is roughly twice as large as the initial bandwidth, which is defined by the monochromator bandwidth. This is a result of the longer wavelength energy and density modulations present along the LPS of the electron beam. Additionally, the higher frequency modulations produces the additional frequency content shown in the figure. These effects conspire to lower the fractional energy which is stored within the primary bandwidth of the FEL pulse, which in turn lowers the overall peak spectral brightness.

SUMMARY AND CONCLUSION

The relatively low energy of the LCLS-II electron beam and the long transport from the linac to the undulators leaves the beam susceptible to a strong space-charge driven microbunching instability, which in turn generates longitudinal variations of the electron beam slice properties. These variations may negatively impact the FEL performance. As such, high fidelity numerical particle simulations have been performed in an attempt to capture the relevant physics and to evaluate the performance of the FEL under these circumstances. Three separate charge distributions were evaluated in both the SXR and HXR undulators across the their full tuning ranges. In addition, time-dependent taper optimizations were performed in order to more accurately characterize an optimal performance. It was found that the MBI induced energy and current variations had only a small impact on the SASE FEL performance while the seeded performance showed the production of a broadband spectral 'pedestal.' Schemes to mitigate the pedestal are currently under investigation.

ACKNOWLEDGMENT

REFERENCES

[1] M. Venturini *et al.*, "The microbunching instability and LCLS-II lattice design: lessons learned", in *These Proceedings: Proc. 37th Int. Free-Electron Laser Conf., Daejeon*, 2015, TUC01.

[2] Z. Zhang *et al.*, "Microbunching-induced sidebands in a seeded free-electron laser", in *These Proceedings: Proc. 37th Int. Free-Electron Laser Conf., Daejeon*, 2015, WEP084.

[3] T. Raubenheimer, "LCLS-II: Status of the CW X-ray FEL Upgrade to the LCLS Facility", in *These Proceedings: Proc. 37th Int. Free-Electron Laser Conf., Daejeon*, 2015, WEP014.

[4] J. Feldhaus *et al.*, *Opt. Comm.* **140**, 341 (1997).

[5] G. Geloni *et al.*, *Journ. Mod. Opt.* **58**, 16 (2011).

[6] T. O. Raubenheimer,"Technical Challenges of the LCLS-II", *in Proceedings: Proc. 6th Int. Part. Acc. Conf., Richmond*, 2015, WEYC1.

[7] G. Marcus, "FEL Simulation and Performance Studies for LCLS-II', *in Proceedings: Proc. 36th Int. Free-Electron Laser Conf., Basel*, 2014, TUP032.

[8] M. Borland *et al.*, *Nucl. Instrum. Methods Phys. Res. Sect. A*, **483**, 268 (2002).

[9] E. L. Saldin *et al.*, *Nucl. Instrum. Methods Phys. Res. Sect. A*, **490**, 1 (2002).

[10] Z. Huang *et al.*, *Phys. Rev. ST Accel. Beams*, **7**, 074401 (2004).

[11] D. Ratner *et al.*, *Phys. Rev. Lett.*, **114**, 054801 (2015).

[12] R. Lindberg, unpublished.

[13] G. Penn *et al.*, "Effect of Microbunching on Seeding Schemes for LCLS-II", in *These Proceedings: Proc. 37th Int. Free-Electron Laser Conf., Daejeon*, 2015, WEP025.

[14] J. Qiang *et al.*, *Phys. Rev. ST Accel. Beams*, **9**, 044204 (2006).

[15] J. Qiang *et al.*, *J. of Comp. Phys.*, **163**, 434 (2000).

[16] J. Qiang *et al.*, *Phys. Rev. ST Accel. Beams*, **12**, 100702 (2009).

[17] S. Reiche, *Nucl. Instr. Meth. Phys. Res. Sec. A* **429**, 243 (1999).

[18] J. Qiang *et al.*, "Start-to-End Simulation of the LCLS-II Beam Delivery System with Real Number of Electrons", in *These Proceedings: Proc. 37th Int. Free-Electron Laser Conf., Daejeon*, 2015, WEP070.

[19] Y. Jiao *et al.*, *Phys. Rev. ST Accel. Beams*, **15**, 050704 (2012).

[20] W. M. Fawley, *Nucl. Instr. Meth. Phys. Res. Sec. A* **483**, 537 (2002).

[21] Y. Feng *et al.*, "System Design for Self-Seeded the LCLS at Soft X-ray Energies", in *Proc. 34th Int. Free-Electron Laser Conf.*, Nara, 2012, TUoBI01.

[22] G. Marcus, *to be published*